ADVANCED ELECTRONIC MATERIALS Open Access
www.advelectronicmat.de

Pressure-Induced Volumetric Negative Thermal Expansion in $CoZr_2$ Superconductor

*Yuto Watanabe, Hiroto Arima, Saori Kawaguchi-Imada, Hirokazu Kadobayashi, Kenta Oka, Hidetomo Usui, Ryo Matsumoto, Yoshihiko Takano, Takeshi Kawahata, Chizuru Kawashima, Hiroki Takahashi, Aichi Yamashita, and Yoshikazu Mizuguchi**

The study investigates the thermal expansion and superconducting properties of a $CuAl_2$-type (tetragonal) superconductor $CoZr_2$ under high pressures. High-pressure synchrotron X-ray diffraction is performed in a pressure range of 2.9 GPa < *P* < 10.4 GPa, and it is discovered that $CoZr_2$ exhibits volumetric negative thermal expansion (NTE) under high pressures. Although uniaxial positive thermal expansion (PTE) along the *a*-axis is observed under ambient pressure, it is suppressed by pressure, whereas a large uniaxial NTE along the *c*-axis is maintained under the pressure regime. Because of the combination of the suppressed uniaxial PTE along the *a*-axis and uniaxial NTE along the *c*-axis, volumetric NTE is achieved under high pressure in $CoZr_2$. The volumetric NTE mechanism is based on the flexible crystal structure caused by the soft Co–Co bond, as observed in the isostructural compound $FeZr_2$, which exhibits a uniaxial NTE along the *c*-axis. High-pressure electrical resistance measurements of $CoZr_2$ are performed and confirm superconductivity at 0.03 GPa < *P* < 41.9 GPa. Because of the coexistence of the two phenomena, volumetric NTE and superconductivity, in $CoZr_2$ under high pressure, coexistence can be achieved under ambient pressure by tuning the chemical composition after the present observation.

1. Introduction

Thermal expansion is a phenomenon related to the properties of electrons and phonons. In most cases, materials expand upon heating; this conventional property is known as positive thermal expansion (PTE). In contrast, negative thermal expansion (NTE) is defined as contraction upon heating, and has been observed in various materials.[1–4] The mechanisms of NTE are diverse and correlated with the flexible crystal structure,[5,6] phase transition,[7] and magnetic order-to-disorder transition.[8] NTE has been used to achieve zero thermal expansion in practical devices by fabricating composites of PTE and NTE. In superconducting devices, the heat cycle between the working temperature below the superconducting transition temperature and room temperature when the device is turned off is a critical issue because the heat cycle degrades the surface and junction between materials with different coefficients of thermal expansion. If a superconductor with an NTE or zero-thermal expansion (ZTE) exists in a wide temperature range below the room temperature, the heat-cycle problem will improve. Isotropic and uniaxial NTE has been reported in various superconducting materials, such as single elements Nb[9,10] and Ta,[10] layered materials MgB_2,[9,11] $YBa_2Cu_3O_{7-\delta}$,[12]

Y. Watanabe, H. Arima, A. Yamashita, Y. Mizuguchi
Department of Physics
Tokyo Metropolitan University
1-1, Minami–Osawa, Hachioji 192-0397, Japan
E-mail: mizugu@tmu.ac.jp

S. Kawaguchi-Imada, H. Kadobayashi, K. Oka
Japan Synchrotron Radiation Research Institute (JASRI)
1-1-1 Koto, Sayo-cho, Sayo-gun, Hyogo 679-5198, Japan

H. Usui
Department of Applied Physics
Shimane University
Matsue, Shimane 690-8504, Japan

R. Matsumoto, Y. Takano
International Center for Materials Nanoarchitectonics (MANA)
National Institute for Materials Science
Tsukuba, Ibaraki 305-0047, Japan

T. Kawahata, C. Kawashima, H. Takahashi
Department of Physics
College of Humanities and Sciences
Nihon University
Setagaya, Tokyo 1568550, Japan

The ORCID identification number(s) for the author(s) of this article can be found under https://doi.org/10.1002/aelm.202300896

DOI: 10.1002/aelm.202300896

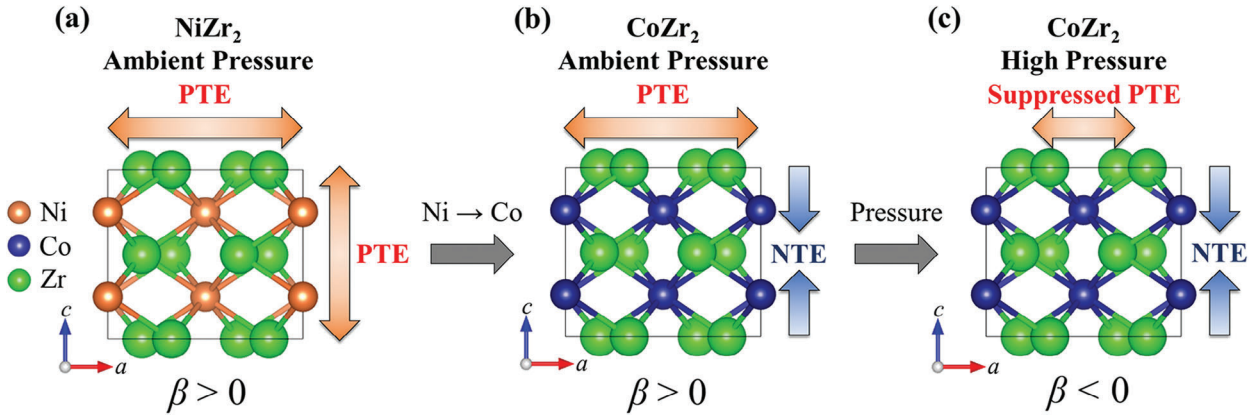

Figure 1. Schematic images of thermal expansion of a) $NiZr_2$, b) $CoZr_2$, and c) $CoZr_2$ under high pressures.

$Bi_2Sr_2CaCu_2O_{8+x}$,[13] PrFeAsO,[14] and $Ba(Fe_{1-x}Co_x)_2As_2$ (x = 0.16, 0.23).[15] Those NTEs were observed over a limited temperature range, and volumetric NTE over a wide temperature range have not been achieved in bulk superconducting materials.

Recently, we observed a uniaxial NTE along the *c*-axis over a wide temperature range in the $CuAl_2$-type (tetragonal) superconductors *Tr*Zr_2 and *Tr*Zr_3 (*Tr*: transition metal).[16–18] In the *Tr*Zr_2 system, we revealed that the uniaxial NTE along the *c*-axis can be controlled by the lattice constant ratio c/a, through chemical element substitution.[19,20] The sign of the linear coefficient of thermal expansion along the *c*-axis changes from positive to negative upon the substitution of Ni with Co at ambient pressure.[20] The anomalous bonding states related to the uniaxial NTE along the *c*-axis in *Tr*Zr_2 have also been observed using X-ray absorption spectroscopy.[21] Moreover, Xu et al. revealed that $FeZr_2$ exhibits a giant uniaxial NTE along the *c*-axis and proposed that the soft Fe–Fe bond and flexible structure caused by optical phonons play an important role in the origin of the uniaxial NTE along the *c*-axis.[22] The absence of NTE along the *c*-axis for $NiZr_2$ is related to the stiff bonds between the Ni atoms derived from antibonding interactions. Therefore, crystal structure modification is critical for the NTE phenomenon in *Tr*Zr_2.

Herein, we report the observation of volumetric NTE in $CoZr_2$ under high pressure. At ambient pressure, $CoZr_2$ exhibits superconductivity at T_c = 5.8 K (T_c: superconducting transition temperature), uniaxial PTE along the *a*-axis, and uniaxial NTE along the *c*-axis. The uniaxial PTE along the *a*-axis was suppressed by pressure, whereas the uniaxial NTE along the *c*-axis was not suppressed by pressure. As a consequence of the competition between uniaxial PTE and NTE along the *a*- and *c*-axes, the volumetric NTE was realized under pressure because of $\beta = 2\alpha_a + \alpha_c$, as expressed in Equation (1). Because the coexistence of superconductivity and volumetric NTE over a wide temperature range is rare, we confirmed the presence of superconductivity in $CoZr_2$ under high pressure using electrical resistance measurements.

2. Results and Discussion

2.1. Thermal Expansion under High Pressure

We show the schematic images of the thermal expansions of the structural analogs $NiZr_2$ and $CoZr_2$ (under ambient and high pressures) in **Figure 1**. These compounds have tetragonal $CuAl_2$-type crystal structures (space group: $I4/mcm$). $NiZr_2$ exhibits PTE both along the *a*- and *c*-axes, and thus, the coefficient of volumetric thermal expansion β is positive (Figure 1a).[19,20] In the tetragonal crystal structure, β can be calculated according to the following equation:

$$\beta = 2\alpha_a + \alpha_c \quad (1)$$

where α_a and α_c denote the coefficients of linear thermal expansion along the *a*- and *c*-axes, respectively. In contrast to $NiZr_2$, $CoZr_2$ exhibited a uniaxial NTE along the *c*-axis (Figure 1b).[16] For $CoZr_2$, α_a and α_c at ambient pressure are 21.5 ± 0.6 and −17.8 ± 0.5 μK^{-1}, respectively. Therefore, we obtain β = 25 ± 1 μK^{-1} (see Figure S1, Supporting Information). As discussed later, under high pressures, we find that the uniaxial PTE along the *a*-axis is suppressed, but uniaxial NTE along the *c*-axis is not suppressed. Consequently, β could be a negative value, implying that volumetric NTE is realized in $CoZr_2$ under pressure (Figure 1c).

To investigate the thermal expansion properties at high pressure, high-pressure synchrotron X-ray diffraction (HP-SXRD) was performed using a diamond anvil cell (DAC). **Figure 2a** shows the HP-SXRD patterns obtained at T = 303 K at P = 2.9, 5.0, 6.7, 7.4, and 10.4 GPa. The crystal structure remains tetragonal $CuAl_2$-type up to P = 10.4 GPa. We observed a shift in the 002 and 220 peaks toward higher angles upon applying pressure, as shown in Figure 2b,c. The shifts in the peaks resulted in decreasing lattice constants *a* and *c*. Figure 2d shows the pressure dependence of the lattice constants. The lattice constants normalized by the values at ambient pressure (a_0 and c_0) are shown in Figure 2e. The *a*-axis is stiffer than the *c*-axis under high pressure. This implies that the crystal structure of $CoZr_2$ along the *c*-axis is more flexible under pressure. The same trend of *a* and *c* against pressure was also observed in laboratory experiments, which were conducted using another DAC with a Mo–Kα radiation (see Figure S2, Supporting information). As mentioned in the Introduction section, $FeZr_2$, which is an isostructural compound of $CoZr_2$ and $NiZr_2$, exhibits a large uniaxial NTE along the *c*-axis.[22] They revealed that the strong Fe3dz^2–Fe3dz^2 interaction can play an important role in stabilizing the large c/a in the $CuAl_2$-type crystal structure and contributes to the soft Fe–Fe bond, which provides a large contraction space along the *c*-axis.

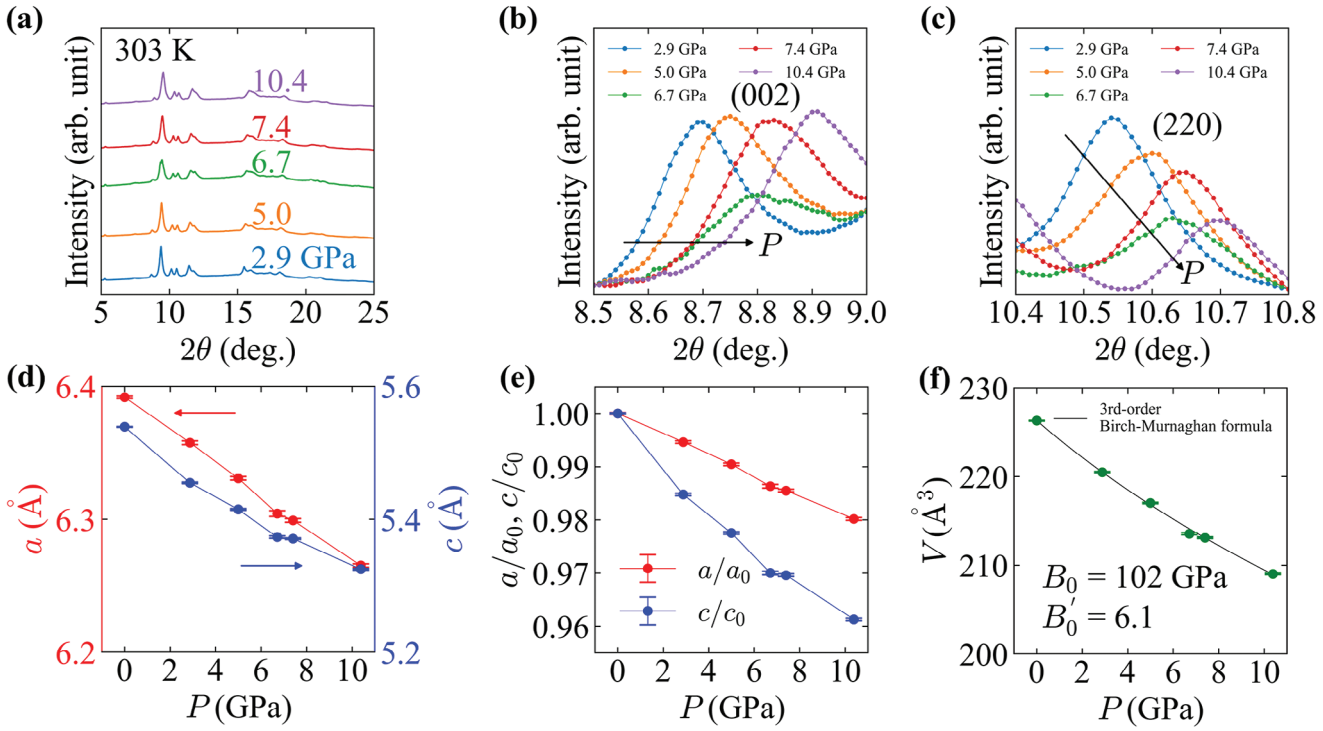

Figure 2. a) HP-SXRD patterns at $T = 303$ K for $CoZr_2$. b,c) Shift of 002 and 220 peaks owing to pressure. Pressure dependence of d) lattice constants a and c and e) a and c normalized by a value at ambient pressure. f) Lattice volume V. The solid line is fit to the third-order Birch–Murnaghan formula.

Furthermore, optical phonons with a phonon energy of several millielectronvolts create a flexible structure in $FeZr_2$, resulting in a giant uniaxial NTE along the c-axis. These flexible characteristics of the crystal structure are common to $CoZr_2$ because they have the same crystal structure with a similar c/a ratio to that of $FeZr_2$ and exhibit a large uniaxial NTE along the c-axis. Figure 2f shows the pressure dependence of lattice volume V of $CoZr_2$. The solid line represents the fit to the third-order Birch–Murnaghan formula, expressed by the following equation:[23]

$$P = \frac{3}{2} B_0 \left\{ \left(\frac{V_0}{V}\right)^{\frac{7}{3}} - \left(\frac{V_0}{V}\right)^{\frac{5}{3}} \right\} \left\{ 1 + \frac{3}{4}\left(B_0' - 4\right) \left[\left(\frac{V_0}{V}\right)^{\frac{2}{3}} - 1 \right] \right\} \quad (2)$$

where V_0, B_0, and B_0' denote the volumes at ambient pressure, bulk modulus, and the first-order pressure derivative of B_0, respectively. As the fitting result, we obtain $B_0 = 102 \pm 3$ GPa and $B_0' = 6.1 \pm 0.8$. The obtained B_0 value was close to the computational results of $B_0 = 134.81$[24] and 129 GPa.[25] Notably, the third-order Birch–Murnaghan formula assumes a cubic structure; thus, the obtained B_0 values can deviate from the actual values.

Next, we show the results of the thermal expansion of $CoZr_2$ at $P = 2.9$ GPa as an example of a high-pressure dataset. For all experiments under pressure, we evaluated the fluctuation in the applied pressures because thermal expansion is easily affected by pressure changes. The data presented in this study were carefully obtained in this manner. **Figure** 3a shows the HP-SXRD patterns at $P = 2.9$ GPa at temperatures ranging from $T = 303$ to 453 K in increments of 10 K. There was no crystal structural transition in the temperature region ($P = 2.9$ GPa, which was commonly confirmed at all other applied pressures (see Figure S3, Supporting Information). The absence of a crystal structural transition at ambient pressure was confirmed over a wide temperature range (7 K < T < 572 K) in ref. [16]. As the temperature increased, a clear shift in the 002 peak toward higher angles was observed, as shown in Figure 3b. However, the position of the 220 peak was almost the same as that of the pressure, as shown in Figure 3c. The robustness of the a-axis to pressure observed from the 220 peak results in a small value of $\alpha_a = 9 \pm 1\ \mu K^{-1}$, which is clearly smaller than that at ambient pressure (see Figure S1, Supporting Information). Figure 3d,e show the temperature dependence of a and c, respectively, at $P = 2.9$ GPa. Even under pressure, the large c-axis NTE is present with $\alpha_c = -24 \pm 1\ \mu K^{-1}$, which is almost the same as that observed under ambient pressure. From Equation (1), we obtain $\beta = -6 \pm 2\ \mu K^{-1}$, suggesting the pressure-induced volumetric NTE in $CoZr_2$. Figure 3f shows the temperature dependence of V at $P = 2.9$ GPa. The volume contracted slightly as the temperature increased. The solid line in Figure 3f is a linear fit curve against the temperature and the fitting derived a similar value of β, which was calculated using Equation (1). Almost all the data points were aligned in the linear fitting curve within the error bars.

We summarize the pressure dependence of α_a, α_c, and β in **Figure** 4. When the pressure is applied to $CoZr_2$, the uniaxial PTE along the a-axis is suppressed; thus, α_a under high pressure is lower than at ambient pressure (Figure 4a). In contrast, even under high-pressure conditions, the uniaxial NTE along the c-axis is not suppressed; therefore, α_c is almost independent of pressure (Figure 4b). Above the ambient pressure, the β value can be negative because the impact of uniaxial NTE along the c-axis on the

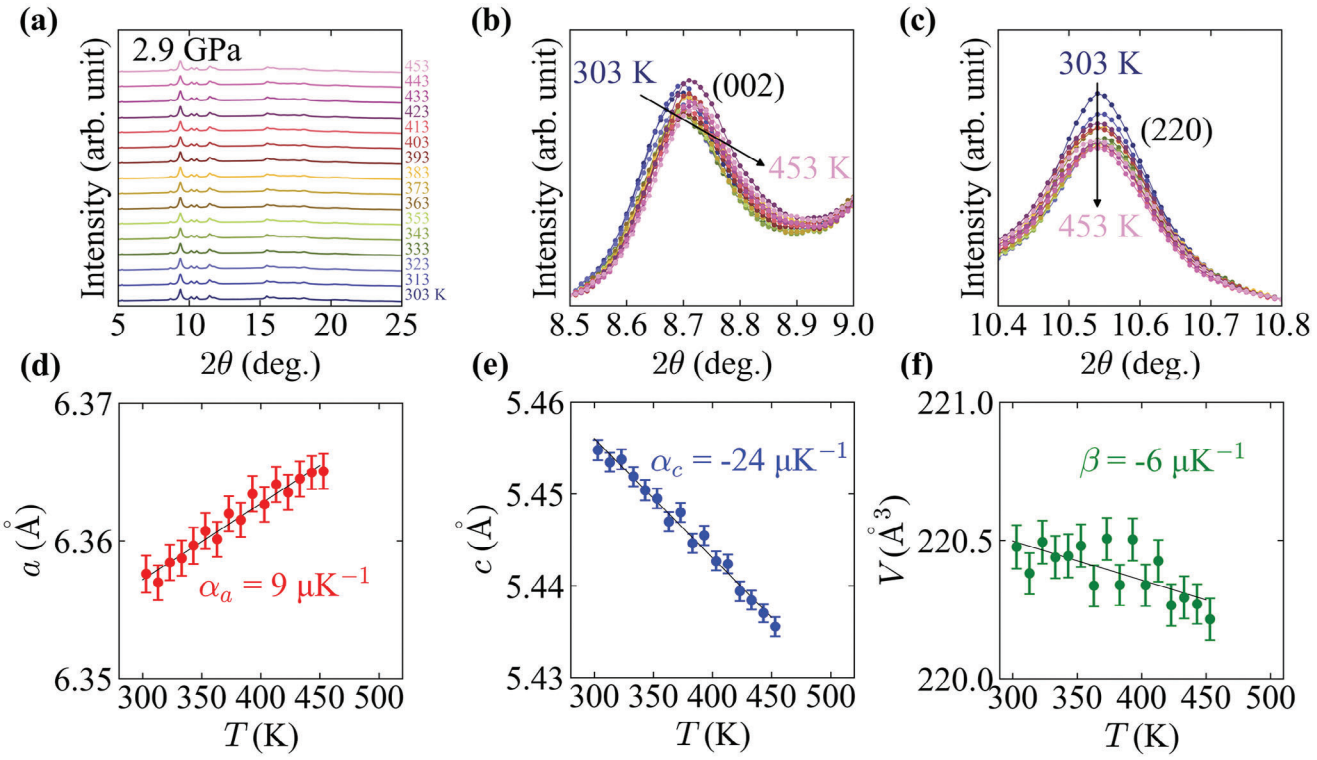

Figure 3. a) HP-SXRD patterns at $P = 2.9$ GPa for $CoZr_2$. b,c) Shift of 002 and 220 peaks owing to heating. Temperature dependence of lattice constants d) *a* and e) *c*. f) Temperature dependence of lattice volume *V*. Solid lines in insets (d–f) are fit to the linear line.

volume exceeds the suppressed uniaxial PTE along the *a*-axis, resulting in volumetric NTE. Unfortunately, we could not conduct pressure experiments between $P = 0$ and 2.9 GPa because of experimental difficulties. However, we expect that the suppression of the uniaxial PTE along the *a*-axis occurs in the low-pressure region. The results of Rietveld refinement of $CoZr_2$ under $P = 2.9$ GPa (303 and 453 K) and $P = 10.4$ GPa (303 and 403 K) are shown in Figure S4 (Supporting information). The results of the same pressure experiment are shown in Figure S5 (Supporting Information). We observe a decreasing trend in volume against temperature under the applied pressures.

2.2. Superconducting Properties

We measured the electrical resistance (*R*) of $CoZr_2$ under high pressures (0.03 GPa < *P* < 41.9 GPa) to confirm the presence of superconductivity. **Figure** 5a,b show the temperature dependence of *R* under pressures. As the temperature decreased, *R*

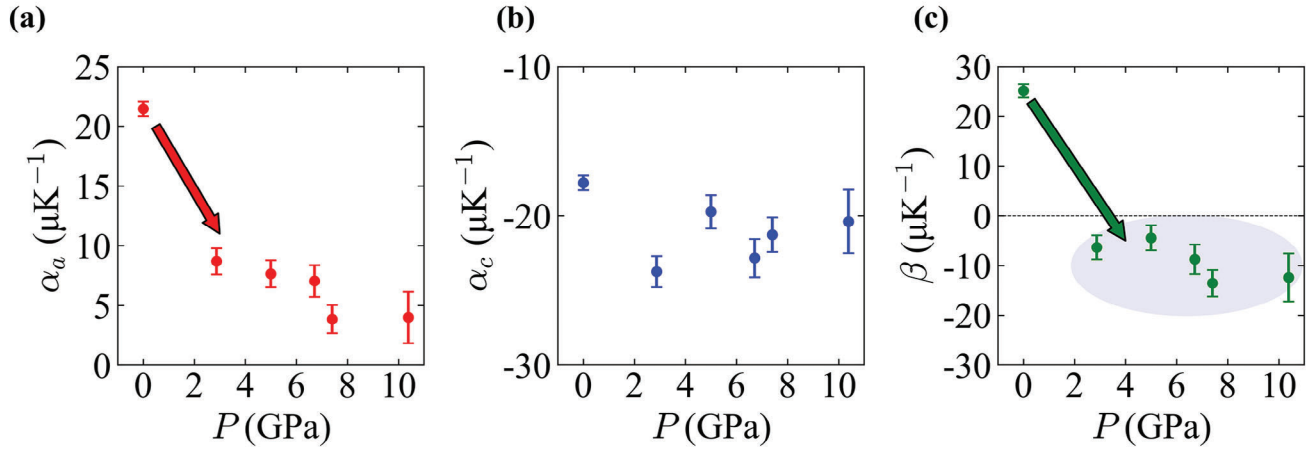

Figure 4. Pressure dependence of the coefficient of linear thermal expansion along the a) *a*-axis α_a and b) *c*-axis α_c. c) Pressure dependence of the coefficient of volumetric thermal expansion β. In the tetragonal crystal structure, β can be calculated as $\beta = 2\alpha_a + \alpha_c$.

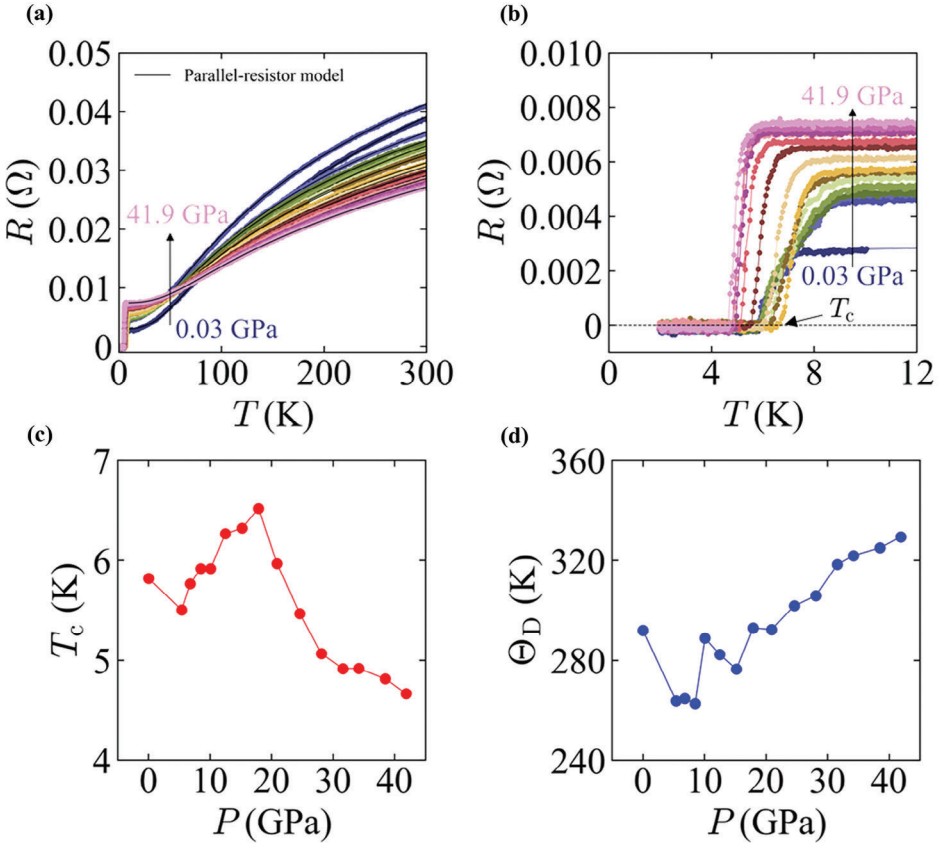

Figure 5. a,b) Temperature dependence of electrical resistance (R) under applied pressures. The solid lines are fit to the parallel-resistor model. c,d) Pressure dependence of superconducting transition temperature T_c and Debye temperature Θ_D.

decreases with a negative curvature, which is a trend commonly observed in *d*-electron superconductors.[26,27] At low temperatures, R drops to zero at T_c under all applied pressures. A dome-shaped pressure dependence of T_c is observed, as shown in Figure 5c. T_c obtained from the R data at ambient pressure (P = 0.03 GPa) was 5.8 K, consistent with the value obtained from magnetic susceptibility measurements at ambient pressure (see Figure S6, Supporting Information). As pressure increases, T_c increases up to P = 17.9 GPa and reaches 6.5 K, but the trend of T_c changed at $P > 17.9$ GPa; T_c decreases with increasing pressure. In a study on a single crystal of $CoZr_2$, T_c reached 9.5 K at P = 8 GPa,[26] which is higher than the highest T_c obtained in this study with polycrystalline $CoZr_2$. The discrepancy in the highest T_c values may be due to the difference in the reactions of T_c to the pressure generated by the experimental conditions, that is, the pressure cells and sample type (single or polycrystalline). In the low-temperature region where $T_c < T \ll \Theta_D$ (Debye temperature), R could be fitted to the power-law relation:

$$R\ (T) = R_0\ + AT^n \tag{3}$$

where R_0 denotes the residual resistance, A denotes a numerical temperature-independent coefficient, and n is a component that depends on the carrier scattering mechanism. We used R at 10 K < T < 30 K under pressures in the fitting to power-law relation, which yielded $n \approx 3$ for all applied pressures as shown in Figure S7 (Supporting information). The T^3 dependence on low-temperature R can be explained with a phonon-assisted *s*–*d* electron scattering model.[28] R of compounds comprising *d*-block elements is empirically known to fit the parallel-resistor model[27,29] developed by Wiesmann et al.[30] In the model, R is described by the following equation:

$$R\ (T) = \left[\frac{1}{R_{sat}\ (T)} + \frac{1}{R_{ideal}\ (T)}\right]^{-1} \tag{4}$$

where R_{sat} denotes the saturated R at high temperatures. Fisk and Webb found that at high temperatures, R of strongly coupled superconducting transition metal compounds, such as Nb_3Sn and Nb_3Sb, saturates at a certain value that corresponds to an electron mean free path of the order of the interatomic spacing in the compound.[31] R_{ideal} comprises the residual electrical resistance R_0 and the phonon-assisted *s*–*d* electron scattering term, as follows:

$$R_{ideal}\ (T) = R_0\ + C\left(\frac{T}{\Theta_D}\right)^3 \int_0^{\frac{\Theta_D}{T}} \frac{x^3}{(e^x - 1)\,(1 - e^{-x})} dx \tag{5}$$

where C denotes a numerical temperature-independent coefficient. We used the R data at 10 K < T < 300 K for fitting to the parallel-resistor model and evaluated the Θ_D values as a function of applied pressure as shown in Figure 5d. The calculated Θ_D is

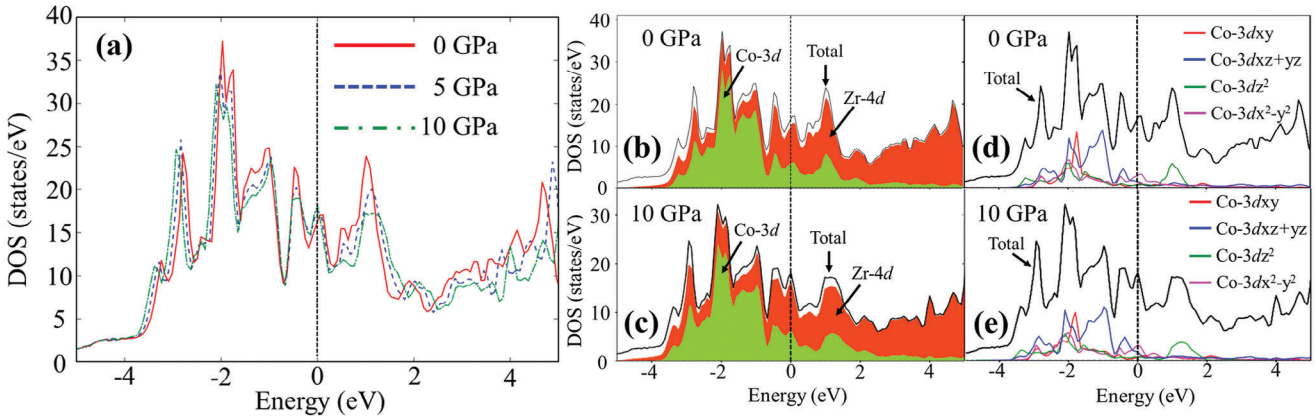

Figure 6. a) Total Electrical DOS for $CoZr_2$ at $P = 0$, 5, and 10 GPa. b,c) Partial DOS for Co-3*d* and Zr-4*d* orbitals at $P = 0$ and 10 GPa, respectively. d,e) Partial DOS for Co-3*dxy*, 3*dxz* + yz, 3dz^2, and 3dx^2-y^2 orbitals at $P = 0$ and 10 GPa, respectively.

292 K at ambient pressure ($P = 0.03$ GPa), which slightly deviates from the value $\Theta_D = 260$ K obtained by another experimental result using specific heat measurement.[32]

As mentioned previously, we observed a dome-shaped pressure dependence of T_c (Figure 5c). In conventional weak-coupling superconductors, T_c can be expressed as follows:[33]

$$T_c = 1.13\Theta_D \exp\left\{-\frac{1}{N(0)\,U}\right\} \quad (6)$$

where $N(0)$ denotes the electronic density of states (DOS) at the Fermi energy and U denotes the effective Coulomb interaction constant. According to Equation (6), T_c is mostly controlled by Θ_D and $N(0)$. Θ_D gradually increases upon applying pressure above 6 GPa (Figure 5d), contributing to an enhancement of T_c. In contrast, $N(0)$ typically decreases under high-pressure conditions because of the expansion of the bandwidth,[34] which contributes to the suppression of T_c. Therefore, the competition of the contributions of Θ_D and $N(0)$ to pairing would cause the dome-shaped pressure dependence of T_c. The dome-shaped pressure dependence of T_c has been observed in other superconductors, such as $CaSb_2$,[35] CsV_3Sb_5,[36] $AuTe_2$,[37] and $Cd_2Re_2O_7$.[38] Possible causes of the discontinuation or dome-shaped pressure dependence of T_c were proposed to be crystal structural transitions or Lifshitz transitions.

Θ_D is related to the elastic properties of the material, particularly the stiffness.[39] As is well known, diamond or crystals with a diamond-type structure whose large Θ_D exhibit a small linear thermal expansion coefficient.[40,41] There would be similar correlation between α_c and Θ_D in $CoZr_2$. However, to clarify the correlation, further experimental and theoretical studies on this phenomenon are needed. The pressure effect on α_c would be negligible because of the Co–Co soft bond similar to the Fe–Fe soft bond observed in $FeZr_2$.[22]

2.3. Electrical Structure

The total electronic DOS and partial DOS are shown in **Figure 6**. The total DOS values near the Fermi energy (E_F) were comparable at $P = 0$, 5, and 10 GPa (Figure 6a). Therefore, the increment trend of T_c below $P = 17.9$ GPa described in Figure 5c may be explained by Θ_D increment. We expect that the decrease in T_c above $P = 17.9$ GPa is due to the reduction in $N(0)$ because the peak near E_F gradually shifted to the low-energy side under rigid band shifting with increasing pressure. The partial DOS for the Co-3*d* and Zr-4*d* orbitals are shown in Figure 6b,c at $P = 0$ and 10 GPa, respectively. The total DOS near E_F mainly comprises Co-3*d* and Zr-4*d* orbitals. Figure 6d,e show the details of Co-3*d* partial DOS at $P = 0$ and 10 GPa, respectively. Most of the partial Co-3*d* DOS are located below E_F at both $P = 0$ and 10 GPa. However, the DOS of the Co-3dz^2 orbital is above E_F, which is an unoccupied state. In the study of $FeZr_2$, the bonding interaction between Fe3dz^2 and Fe3dz^2 contributes to the contraction of the Fe–Fe bond. The Co3dz^2 orbital below E_F should be related to the Co–Co bond contract, similar to that of $FeZr_2$.[22]

Figure 7a shows the charge density isosurfaces of $CoZr_2$ at $P =$ 0, 3, 5, and 10 GPa. As pressure was applied, the charge density of the isosurface between Co–Co and Co–Zr bonds increased, resulting in a decrease in the bond lengths. The Co–Co and Co–Zr bond lengths were reversed at $P = 10$ GPa (Figure 7b). Figure 7c shows the pressure dependence of the bond lengths normalized by the values at ambient pressure. The normalized Co–Co bond length becomes shorter than the normalized Co–Zr bond length under pressure, suggesting that $CoZr_2$ flexibly contracts along the *c*-axis as compared to the *a*-axis, as shown in Figure 2e. A volumetric NTE emerging above $P = 2.9$ GPa would be achieved by changing the bonding state from ambient pressure to $P =$ 2.9 GPa.

3. Conclusion

We measured the temperature-dependent HP-SXRD patterns and the temperature dependence of R on polycrystalline $CoZr_2$ under various pressures. From the HP-SXRD results, we found no crystal structural transition below 10.4 GPa in the measured temperature ranges. The most important result of this study is the discovery of a volumetric NTE induced by the application of high pressure in $CoZr_2$. The uniaxial PTE along the *a*-axis was suppressed by pressure, whereas the uniaxial NTE along the *c*-axis was not. Because of the competition between

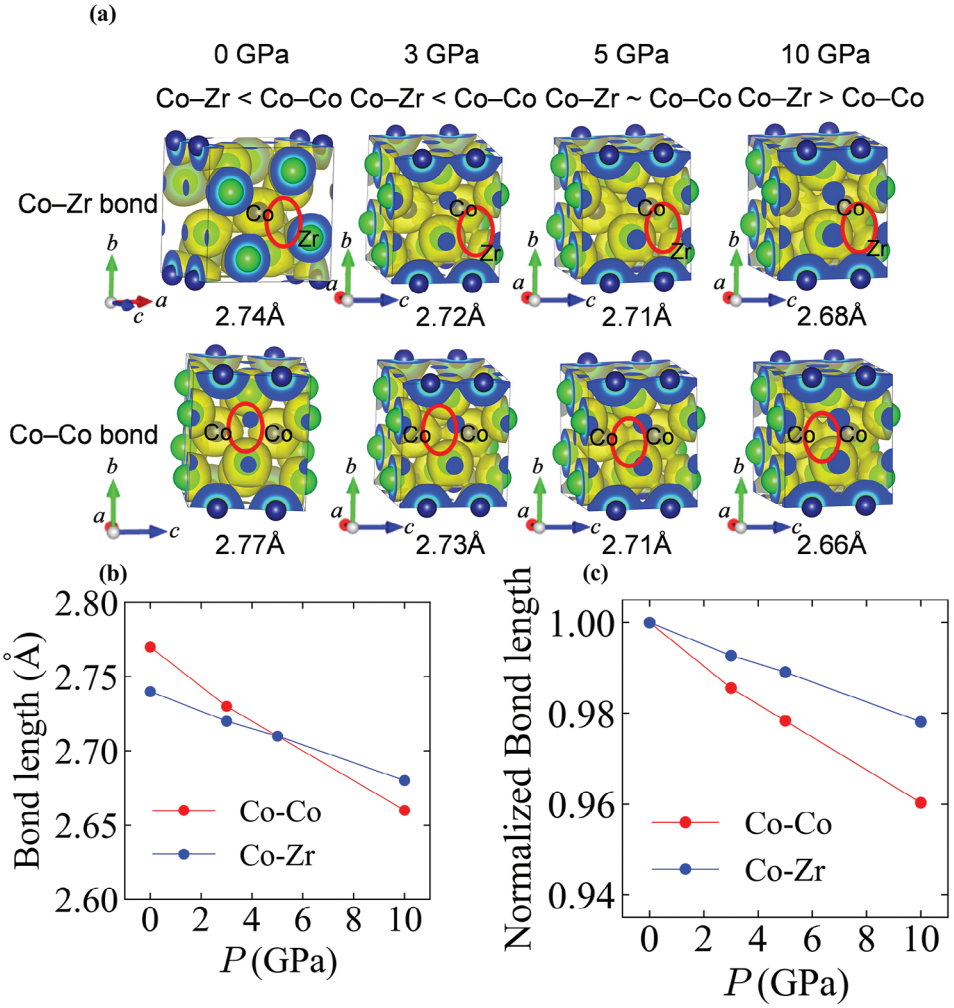

Figure 7. a) Charge density isosurface of $CoZr_2$ at $P = 0$, 3, 5, and 10 GPa. The bond length comparison between Co–Zr and Co–Co is shown at each applied pressure. b) Pressure dependence of Co–Co and Co–Zr bond lengths. c) Bond lengths normalized by a value at ambient pressure.

uniaxial PTE and NTE, volumetric NTE was achieved under high pressures in $CoZr_2$. The robustness of the NTE along the *c*-axis under pressure is related to the flexible crystal structure caused by the soft Co–Co bond proposed in the structural analog $FeZr_2$, which also exhibits a giant uniaxial NTE along the *c*-axis under ambient pressure. The increase in Θ_D against pressure could contribute to the suppression of uniaxial PTE along the *a*-axis. From electronic structure calculations, we found that the Co–Co and Co–Zr bond lengths were reversed at $P = 10$ GPa. The change in the bonding state under pressure is related to the emergence of a unique axis thermal expansion of $CoZr_2$ under high pressures. From pressure–temperature dependences of *R*, we observed the dome-shaped pressure dependence of T_c and an increase of Θ_D with pressure. The dome-shaped pressure dependence of T_c was caused by the competition between the pressure evolutions of Θ_D and $N(0)$. Further investigation of phonon states potentially coupled with uniaxial NTE along the *c*-axis in $CoZr_2$ and its pressure dependence is required to understand the mechanisms of volumetric NTE in $CoZr_2$ under high pressure. Through a systematic investigation of the structural and physical properties of the $CoZr_2$ superconductor, we concluded that $CoZr_2$ exhibits both superconductivity and volumetric NTE, which is possibly maintained in a temperature range lower than room temperature, because the NTE along the *c*-axis was observed over a wide temperature range in a previous study of $CoZr_2$ under ambient pressure. The discovery presented here will lead to material exploration using volumetric NTE under ambient pressure in *Tr*Zr_2 and related superconducting materials.

4. Experimental Section

Sample Preparation: A polycrystalline sample of $CoZr_2$ was prepared using a Co rod (99.98%, Nilaco) and Zr plates (99.2%, Nilaco) via arc melting. The sample chamber was filled with Ar after three gas replacements. The sample was synthesized on a water-cooled Cu stage and turned several times during each melting step for homogenization.

XRD and HP-SXRD Measurements: The laboratory XRD patterns at ambient pressure were measured by the θ–2θ method with Cu–Kα radiation using a Miniflex-600 (RIGAKU) diffractometer equipped with a high-resolution semiconductor detector D/tex-Ultra. The BTS-500 attachment controlled the temperature of the samples. HP-SXRD was measured at the BL10XU beam line of SPring-8 with a wavelength of 0.413278 Å (Proposal

No.: 2023A1254). The sample was loaded into the DAC with a pressure medium (He gas). The actual pressure was determined from the shift in the fluorescence line of ruby R1.[42] A band heater was mounted around the DAC to heat the samples. A K-type thermocouple was placed in the gasket to measure the temperature. The collected laboratory XRD and HP-SXRD patterns were refined by the Rietveld method using RIETAN-FP; site occupancies have been fixed as 1.[43] The images of crystal structures were obtained using VESTA.[44]

Magnetic Susceptibility Measurement: The temperature and field dependences of the magnetic susceptibility were measured using an MPMS3 (Quantum Design), a superconducting quantum interference device magnetometer. The temperature dependence was measured at $\mu_0 H = 1$ mT after both zero-field cooling (ZFC) and field cooling (FC) protocols. The field-dependence was measured at $T = 1.8$ K.

High-Pressure Electrical Resistance Measurement: The T dependence of R under various pressures was investigated using a DAC with boron-doped diamond microelectrodes[45,46] in a PPMS (Quantum design). Cubic BN powder was filled into a hole around a metal gasket (SUS316) as a pressure medium. The generated pressures were determined from the shift in the ruby R1 fluorescence line[42] and Raman peak from the diamond on the culet surface.[47]

First Principles Calculation: First-principles calculations were performed using the VASP software package, employing the projector-augmented wave method.[48–51] The Perdew–Burke–Ernzerhof exchange-correlation functional[52] was used. K-point meshes of $11 \times 11 \times 12$ and $22 \times 24 \times 24$ were utilized for internal coordinate optimization and DOS calculations, respectively. Calculations were performed using experimentally determined lattice constants. A plane-wave cut-off energy of 350 eV was used. Partial DOS was visualized using PyProcar software.[53]

Data Presentation: Coefficients of thermal expansion values are expressed as fitted value ± SD (standard deviation). The fitted value was obtained using the Python curve-fit function. The SD values were calculated according to error propagation rules using error values derived from the fitting.

Supporting Information

Supporting Information is available from the Wiley Online Library or from the author.

Acknowledgements

This work was partly supported by a Grant-in-Aid for Scientific Research (KAKENHI) (Proposal Nos. 21K18834, 23KK0088, and 23K13549), JST-ERATO (JPMJER2201), TMU Research Project for Emergent Future Society, and Tokyo Government-Advanced Research (H31-1).

Conflict of Interest

The authors declare no conflict of interest.

Data Availability Statement

The data that support the findings of this study are available from the corresponding author upon reasonable request.

Keywords

negative volumetric thermal expansion, pressure, superconductor

Received: December 24, 2023
Revised: February 8, 2024
Published online:

[1] J. P. Attfield, *Front. Chem.* **2018**, *6*, 371.
[2] G. D. Barrera, J. A. O. Bruno, T. H. K. Barron, N. L. Allan, *J. Phys.: Condens. Matter.* **2005**, *17*, R217.
[3] J. Chen, L. Hu, J. Deng, X. Xing, *Chem. Soc. Rev.* **2015**, *44*, 3522.
[4] K. Takenaka, *Sci. Tech. Adv. Mater.* **2012**, *13*, 013001.
[5] T. A. Mary, J. S. O. Evans, T. Vogt, A. W. Sleight, *Science* **1996**, *272*, 90.
[6] T. Chatterji, T. C. Hansen, M. Brunelli, P. F. Henry, *Appl. Phys. Lett.* **2009**, *94*, 241902.
[7] J. Zhu, J. Zhang, H. Xu, S. C. Vogel, C. Jin, J. Frantti, Y. Zhao, *Sci. Rep.* **2014**, *4*, 3700.
[8] Y. Song, N. Shi, S. Deng, X. Xing, J. Chen, *Prog. Mater. Sci.* **2021**, *121*, 100835.
[9] G. K. White, *Cryogenics* **1962**, *2*, 292.
[10] A. Hosomichi, Y. Xue, S. Naher, F. Hata, H. Kaneko, H. Suzuki, *J. Phys. Chem. Solids.* **2005**, *66*, 1583.
[11] J. J. Neumeier, T. Tomita, M. Debessai, J. S. Schilling, P. W. Barnes, D. G. Hinks, J. D. Jorgensen, *Phys. Rev. B* **2005**, *72*, 220505.
[12] H. You, U. Welp, Y. Fang, *Phys. Rev. B* **1991**, *43*, 3660.
[13] S. V. Pryanichnikov, S. G. Titova, G. A. Kalyuzhnaya, Y.u. I. Gorina, P. A. Slepukhin, *J. Exp. Theor. Phys.* **2008**, *107*, 69.
[14] S. A. J. Kimber, D. N. Argyriou, F. Yokaichiya, K. Habicht, S. Gerischer, T. Hansen, T. Chatterji, R. Klingeler, C. Hess, G. Behr, A. Kondrat, B. Büchner, *Phys. Rev. B* **2008**, *78*, 140503.
[15] M. S. da Luz, J. J. Neumeier, R. K. Bollinger, A. S. Sefat, M. A. McGuire, R. Jin, B. C. Sales, D. Mandrus, *Phys. Rev. B* **2009**, *79*, 214505.
[16] Y. Mizuguchi, M. R. Kasem, Y. Ikeda, *J. Phys. Soc. Jpn.* **2022**, *91*, 103601.
[17] H. Arima, T. Inui, A. Yamashita, A. Miura, H. Itou, C. Moriyoshi, H. Fujihisa, Y. Mizuguchi, *J. Phys. Soc. Jpn.* **2023**, *92*, 024602.
[18] Y. Mizuguchi, A. Yamashita, *J. Phys. Soc. Jpn.* **2023**, *92*, 074601.
[19] H. Arima, M. R. Kasem, Y. Mizuguchi, *Appl. Phys. Express* **2023**, *16*, 035503.
[20] Y. Watanabe, H. Arima, H. Usui, Y. Mizuguchi, *Sci. Rep.* **2023**, *13*, 1008.
[21] G. M. Pugliese, L. Tortora, G. Tomassucci, R. M. Kasem, T. Mizokawa, Y. Mizuguchi, N. L. Saini, *J. Phys. Chem. Solids.* **2023**, *174*, 111154.
[22] M. Xu, Q. Li, Y. Song, Y. Xu, A. Sanson, N. Shi, N. Wang, Q. Sun, C. Wang, X. Chen, Y. Qiao, F. Long, H. Liu, Q. Zhang, A. Venier, Y. Ren, F. d'Acapito, L. Olivi, D. O. De Souza, X. Xing, J. Chen, *Nat. Commun.* **2023**, *14*, 4439.
[23] F. Birch, *Phys. Rev.* **1947**, *71*, 809.
[24] K. R. Li, W. F. Lu, C. J. Li, D. Şopu, B. Sarac, J. H. Yi, J. Tan, P. Gao, J. Eckert, *Philos. Mag.* **2020**, *100*, 874.
[25] S. F. Matar, *Intermetallics* **2013**, *36*, 25.
[26] A. Teruya, M. Kakihana, T. Takeuchi, D. Aoki, F. Honda, A. Nakamura, Y. Haga, K. Matsubayashi, Y. Uwatoko, H. Harima, M. Hedo, T. Nakama, Y. Ōnuki, *J. Phys. Soc. Jpn.* **2016**, *85*, 034706.
[27] D. A. Mayoh, J. A. T. Barker, R. P. Singh, G. Balakrishnan, D. McK. Paul, M. R. Lees, *Phys. Rev. B* **2017**, *96*, 064521.
[28] A. H. Wilson, *Proc. R. Soc. Lond. A* **1938**, *167*, 580.
[29] Y. Qi, J. Guo, H. Lei, Z. Xiao, T. Kamiya, H. Hosono, *Phys. Rev. B* **2014**, *89*, 024517.
[30] H. Wiesmann, M. Gurvitch, H. Lutz, A. Ghosh, B. Schwarz, M. Strongin, P. B. Allen, J. W. Halley, *Phys. Rev. Lett.* **1977**, *38*, 782.
[31] Z. Fisk, G. W. Webb, *Phys. Rev. Lett.* **1976**, *36*, 1084.
[32] M. R. Kasem, A. Yamashita, T. Hatano, Y. Goto, O. Miura, Y. Mizuguchi, *Supercond. Sci. Technol.* **2021**, *34*, 125001.
[33] J. Bardeen, L. N. Cooper, J. R. Schrieffer, *Phys. Rev.* **1957**, *108*, 1175.
[34] T. F. Smith, C. W. Chu, *Phys. Rev.* **1967**, *159*, 353.
[35] S. Kitagawa, K. Ishida, A. Ikeda, M. Kawaguchi, S. Yonezawa, Y. Maeno, *Phys. Rev. B* **2021**, *104*, L060504.
[36] Z. Zhang, Z. Chen, Y. Zhou, Y. Yuan, S. Wang, J. Wang, H. Yang, C. An, L. Zhang, X. Zhu, Y. Zhou, X. Chen, J. Zhou, Z. Yang, *Phys. Rev. B* **2021**, *103*, 224513.

[37] S. Kitagawa, H. Kotegawa, H. Tou, H. Ishii, K. Kudo, M. Nohara, H. Harima, *J. Phys. Soc. Jpn.* **2013**, *82*, 113704.
[38] T. C. Kobayashi, Y. Irie, J. Yamaura, Z. Hiroi, K. Murata, *J. Phys. Soc. Jpn.* **2011**, *80*, 023715.
[39] T. Tohei, A. Kuwabara, F. Oba, I. Tanaka, *Phys. Rev. B* **2006**, *73*, 064304.
[40] P. Jacobson, S. Stoupin, *Diam. Relat. Mater.* **2019**, *97*, 107469.
[41] D. F. Gibbons, *Phys. Rev.* **1958**, *112*, 136.
[42] H. K. Mao, P. M. Bell, J. W. Shaner, D. J. Steinberg, *J. Appl. Phys.* **2008**, *49*, 3276.
[43] F. Izumi, K. Momma, *Solid State Phenom.* **2007**, *130*, 15.
[44] K. Momma, F. Izumi, *J. Appl. Crystallogr.* **2011**, *44*, 1272.
[45] R. Matsumoto, Y. Sasama, M. Fujioka, T. Irifune, M. Tanaka, T. Yamaguchi, H. Takeya, Y. Takano, *Rev. Sci. Instrum.* **2016**, *87*, 076103.
[46] R. Matsumoto, T. Irifune, M. Tanaka, H. Takeya, Y. Takano, *Jpn. J. Appl. Phys.* **2017**, *56*, 05FC01.
[47] Y. Akahama, H. Kawamura, *J. Appl. Phys.* **2004**, *96*, 3748.
[48] G. Kresse, J. Hafner, *Phys. Rev. B* **1993**, *47*, 558.
[49] G. Kresse, J. Furthmüller, *Comput. Mat. Sci.* **1996**, *6*, 15.
[50] G. Kresse, J. Furthmüller, *Phys. Rev. B* **1996**, *54*, 169.
[51] G. Kresse, D. Joubert, *Phys. Rev. B* **1999**, *59*, 1758.
[52] J. P. Perdew, K. Burke, M. Ernzerhof, *Phys. Rev. Lett.* **1996**, *77*, 3865.
[53] U. Herath, P. Tavadze, X. He, E. Bousquet, S. Singh, F. Muñoz, A. H. Romero, *Comput. Phys. Commun.* **2020**, *251*, 107080.